communications chemistry

A Nature Portfolio journal

Article

https://doi.org/10.1038/s42004-026-02236-8

The energetics of high temperature oxidation and formation mechanisms in binary lanthanide nitrides (*Ln*N)

Check for updates

P. Uhlemann[1] ✉, W. Vance[2], M. P. Heaney[2], N. Yaw[2], C. Schreinemachers[1], P. Kegler[1], P. Höhn[3], X. Guo[2] ✉, G. Modolo[1] & G. L. Murphy[1] ✉

Nitride-based materials present exceptional thermal and structural properties for advanced material applications, however accurate determination of their thermodynamic properties is critical to their deployment. Herein, the standard enthalpies of formation, ΔH_f°, for all *Ln*N compounds (*Ln* = La, Ce, Pr, Nd, Sm, Eu, Gd, Tb, Dy, Ho, Er, Tm, Lu; excluding Pm) are determined via high temperature oxide melt calorimetry. These measurements are supported by high temperature oxidation studies of La, Ce, Sm, Eu, Er, Yb bearing *Ln*N compounds using X-ray diffraction and thermogravimetric analysis, and are cross-examined against recent high temperature measurements on other *Ln*N compounds[1]. It was determined that ΔH_f° systematically correlates with the ionic radius of Ln^{3+} cations, with smaller *Ln* bearing nitrides having more negative values. A discontinuity in ΔH_f° was further observed between larger and smaller *Ln* bearing *Ln*N compounds. Using the determined ΔH_f° values with literature references, Gibbs energies of formation (ΔG_f°), oxidation (ΔG_{ox}°) and hydrolysis (ΔG_{hyd}°) are calculated and compared against uranium nitride (UN) in the context of UN based nuclear fuel and related spent nuclear fuel (SNF) management. The calculations indicate that the occurrence of *Ln*N phases within UN based SNF should lead to stabilisation of the structure and inhibit its oxidation.

Binary lanthanide nitrides (*Ln*N) are an important class of inorganic compounds that are relevant to spintronic devices[2,3], heterogeneous catalysis[4,5], high-temperature applications[6,7] and are also expected to form an important constituent within next-generation uranium nitride (UN) based spent nuclear fuel (SNF)[8–10]. The use of nitrides in nuclear energy applications arises from their improved density and higher thermal conductivity, while still providing a higher melting point over conventional oxide fuel. This has subsequently drawn considerable interest in these materials to be deployed in Generation IV fast and advanced modular reactors (AMR)[11–15], as part of general interest in advanced fuel concepts[14,16,17]. Critically, mixed *Ln*N-UN compounds are expected to form as a predominant matrix incorporated fission product phase in UN-based SNF, which may affect its chemical stability[9,18,19]. Consequently, the understanding of their thermodynamic stability and precise oxidation behaviour is critical to their application and occurrence in nuclear and non-nuclear applications.

Thermodynamic investigations of *Ln*N and UN SNF relevant materials have primarily been achieved via computational simulation-based methods[8,20,21]. However, the success of computational methods requires precise experimental data, such as high-quality thermodynamic data, for benchmarking. For UN, its enthalpy of formation[22] has been determined via high-temperature oxide melt calorimetry, considered the gold standard for this determination. In comparison, thermodynamic data of *Ln*N compounds remain limited. The standard enthalpy of formation (ΔH_f°) has been measured for some *Ln*N compounds (*Ln* = La, Ce, Sm, Eu, Gd, Ho, Er, Yb) via Knudsen effusion mass spectrometry (KEMS)[22–25].

A challenging component of *Ln*N and UN characterisation is their strong susceptibility to oxidation when in contact with atmospheric oxygen or water. This causes the materials to rapidly oxidise and compromises the measurement. It has been recently shown that under ambient conditions, UN and *Ln*N compounds oxidise under dissimilar mechanisms in which UN follows a direct O_2 oxidation pathway, whereas *Ln*N compounds decompose through hydrolysis (H_2O)[1]. At higher temperatures, the oxidation of *Ln*N compounds proceeds to the sesquioxide, Ln_2O_3, (*Ln* = Nd, Gd, Dy, Ho, Tm, Lu), or dioxide, LnO_2, (*Ln* = Pr, Tb)[1]. In the case of UN, at high temperatures (>200 °C), it oxidises directly via ignition to U_3O_8[26,27].

[1]Institute of Fusion Energy and Nuclear Waste Management (IFN-2), Forschungszentrum Jülich GmbH, Jülich, Germany. [2]Department of Chemistry, Alexandra Navrotsky Institute for Experimental Thermodynamics, Washington State University, Pullman, WA, USA. [3]Max-Planck-Institute for Chemical Physics of Solids, Dresden, Germany. ✉e-mail: p.uhlemann@fz-juelich.de; x.guo@wsu.edu; g.murphy@fz-juelich.de

Despite the strong foundation of knowledge for UN, the discordant behaviour of *Ln*N compounds in terms of their oxidation chemistry demands thorough investigation.

Considering the pertinence of *Ln*N compounds to advanced material applications and also UN-based SNF, the present investigation has experimentally determined ΔH_f° for all *Ln*N compounds (*Ln* = La, Ce, Pr, Nd, Sm, Eu, Gd, Tb, Dy, Ho, Er, Tm, Yb and Lu, excluding Pm) using high-temperature oxide melt calorimetry. The high-temperature oxidation behaviour of *Ln*N for *Ln* = La, Ce, Sm, Eu, Er and Yb has been further characterised by thermogravimetric measurements and compared with recent measurements of *Ln* = Pr, Nd, Gd, Tb, Dy, Ho, Tm and Lu[1]. Structural characterisation of synthesised *Ln*N materials and their respective oxidation products was carried out using powder X-ray diffraction (PXRD) with Rietveld analysis. Using the ΔH_f° values determined and combining with literature references, the Gibbs energies of formation (ΔG_f°), oxidation (ΔG_{ox}°) and hydrolysis (ΔG_{hyd}°) were calculated in comparison to UN in order to gain insight into the relative stability and behaviour of *Ln*N and UN compounds occurring in UN-based SNF. These results of the investigation are further discussed in relation to previous simulation studies and in relation to the oxidation stability of these *Ln*N and UN compounds in relation to associated SNF.

Results and discussion

High temperature oxidation of LnN

Pristine *Ln*N powders synthesised in this work and their respective oxidation residues after heating in synthetic air at 900 °C were measured via PXRD and analysed using the Rietveld refinement method. Pristine *Ln*N samples could be consistently refined against a cubic face-centred structure in space group $Fm\bar{3}m$, isostructural with rock salt. The refinement profiles and diffractograms for pristine *Ln*N compounds (*Ln* = La, Ce, Sm, Eu, Er, Yb) are shown in Fig. 1 with refinement results summarised in Table 1, whereas the results for *Ln*N (*Ln* = Pr, Nd, Gd, Tb, Dy, Ho, Tm and Lu) have been previously reported and discussed in detail[1].

It was found that the determined lattice parameters from Rietveld analysis were in agreement with structural data reported in the literature[28–32], with small deviations attributed to non-stoichiometry in the nitrogen content of synthesised *Ln*N phases. Slight impurities of $La(OH)_3$ have been observed solely in the LaN sample with 5.51 wt% and crystallising in hexagonal $P6_3/m$ structure, which is attributed to slight oxidation arising from contact with atmospheric water during the PXRD measurement. This water-mediated oxidation behaviour of *Ln*N compounds was recently investigated[1], where it was shown that the Ln^{3+}N compounds with larger and lighter *Ln*'s cations oxidised faster than the nitrides with smaller and heavier *Ln* cations.

To accurately determine ΔH_f° via high-temperature oxide melt calorimetry of the investigated *Ln*N compounds, their high-temperature oxidation mechanisms are required to be established. Recent studies[1] in oxygen-containing atmospheres up to 900 °C for *Ln* = Pr, Nd, Gd, Tb, Dy, Ho, Tm and Lu show that these materials oxidise via two pathways to the respective Ln_2O_3 (*Ln* = Nd, Gd, Dy, Ho, Tm, Lu) and LnO_2 oxide compounds (*Ln* = Pr, Tb). Their reactions are described according to Eqs. (1) and (2).

$$LnN + \frac{3}{4}O_2 \rightarrow \frac{1}{2}Ln_2O_3 + \frac{1}{2}N_2 \quad (1)$$

$$LnN + O_2 \rightarrow LnO_2 + \frac{1}{2}N_2 \quad (2)$$

With respect to the literature, *Ln*N compounds for *Ln* = La, Ce, Sm, Eu, Er, Yb have not been investigated under similar conditions to those of the present investigation and necessary for a calorimetric study. It has been previously suggested that ErN forms Er_2O_3 under oxidising conditions, but details are lacking on the precise temperature at which the transformation occurs[33]. To address this, coupled TGA-DSC measurements were performed on these *Ln*N compounds (*Ln* = La, Ce, Sm, Eu, Er, Yb), where powder samples were heated to 900 °C in synthetic air, and the residues after oxidation were characterised via PXRD. Rietveld profiles made against the PXRD data are presented in the inset to their respective *Ln*N phases in Fig. 1. The analysis revealed that all *Ln*N compounds investigated follow an oxidation pathway as given by Eqs. (1) or (2). Refined lattice parameters of the oxidised *Ln*N phases are summarised in Table 2 and are in agreement with the lattice parameters reported in the literature.

Simultaneous TGA and DSC measurements were performed from room temperature to 900 °C under flowing air conditions for the *Ln*N compounds with *Ln* = La, Ce, Sm, Eu, Er and Yb. These were performed to ensure consistency with previous measurements taken under similar conditions[1]. The resulting profiles are displayed in Fig. 2, where the TGA data were normalised against the fully oxidised *Ln*N compounds that were recovered after cooling. This has been performed since the pristine *Ln*N exhibits varying stoichiometries at room temperature, compromising sum formula calculations based on the weight change. All determined and calculated TGA and DSC results are summarised in Table 3. It was found that all *Ln*N compounds oxidise in a direct oxygen-mediated reaction following the reactions shown in Eqs. (1) and (2), consistent with previous investigation[1]. However, it must be noted that the oxidation of CeN proceeds via an observable intermediate oxide, whose composition could be determined approximately as $CeO_{1.80}$. The formation of a distinct intermediate can be attributed to the intrinsic tendency of Ce to form mixed-valence oxidation states of +3 and +4 in oxide form, which is also observed for PrN and TbN[1].

High temperature oxide melt calorimetry

High-temperature oxide melt calorimetric measurements were conducted on all *Ln*N (*Ln* = La, Ce, Pr, Nd, Sm, Eu, Gd, Tb, Dy, Ho, Er, Tm, Yb, Lu; excluding Pm) compounds to determine their standard enthalpies of formation ΔH_f°. Two thermochemical cycles which are provided in Table 4 and Table 5 have been developed based on the oxidation pathways shown in Eqs. (1) and (2), which were used to calculate ΔH_f° based on the measured dissolution enthalpies, (ΔH_{ds}) of *Ln*N in sodium molybdate at 973 K. Experimental ΔH_{ds} data are summarised in Supplementary Information Note 3, Table S3 together with literature enthalpies of the corresponding *Ln* oxides used for calculation. The resulting ΔH_f° values of the *Ln*N compounds examined in this investigation are summarised in Table 6 with their associated standard error. Error propagation with the two standard errors of the dissolution enthalpies $2\sigma(\Delta H_{ds})$ (summarised in Supplementary Information Note 3, and Table S3) and standard errors of the published literature data (summarised in Supplementary Information Note 3, and Table S3) has been performed for all datasets. The dataset of CeN was corrected for the TiO_2 encapsulation used to protect the sample against premature ignition using appropriate literature values[34].

Figure 3 provides the determined ΔH_f° of all *Ln*N compounds plotted against the ionic radii of Ln^{3+} cations in sixfold coordination[35]. The Figure pertinently shows that the *Ln*N compounds that possess smaller and heavier *Ln* cations exhibit lower ΔH_f°, whereas those with larger and lighter *Ln* cations show less negative values. The data of heavy *Ln*'s contrasts significantly with previously determined ΔH_f° values based on KEMS investigation[23–25], which suggests largely consistent values of ΔH_f° in the range of −300 to −350 kJ mol^{-1} and is plotted for comparison in Supplementary Information Note 3, and Fig. S2.

Additionally, the determined ΔH_f° values for the *Ln*N compounds exhibit a discontinuity in the enthalpy trend between TbN and DyN, separating the series into lighter *Ln* (La, Ce, Pr, Sm, Eu, Gd, Tb) with higher ΔH_f°, and heavier *Ln* (Dy, Ho, Er, Tm, Yb, Lu) with lower ΔH_f°. This break is consistent with the half-filling of the 4*f* orbitals, due to which *Ln*N containing heavier *Ln* cations exhibit higher stability compared to *Ln*N containing lighter *Ln* cations. However, Tb is a notable exception to the trend in Fig. 3. Such a deviation could be related to a potential covalent contribution to the bond in TbN, attributable to mixed ionic and covalent bonding

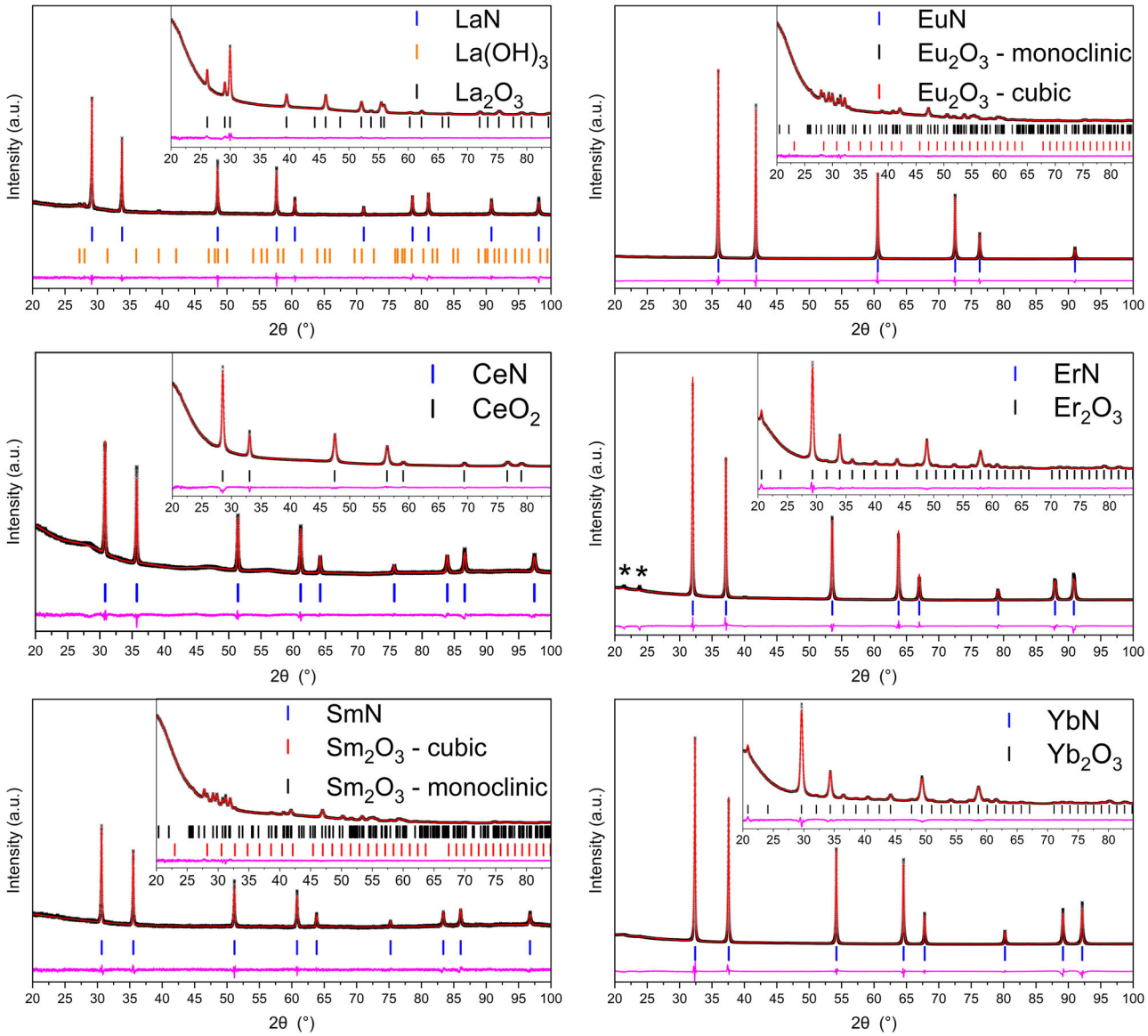


Fig. 1 | Pre- and post-oxidation PXRD comparison of investigated *Ln*N compounds. Rietveld profiles made against PXRD data of pristine *Ln*N (*Ln* = La, Ce, Sm, Eu, Er, Yb) compounds. The insets provide corresponding Rietveld profiles for the same samples oxidised in synthetic air at 900 °C. The black crosses correspond to collected data for the pre- and post-oxidised samples. The red and pink lines correspond to the calculated and difference profiles. The vertical markers correspond to the allowed reflections according to the space group of *Ln*N crystallising in cubic $Fm\bar{3}m$ structure marked in blue, Ln_2O_3/LnO_2 crystallising in varying hexagonal, cubic and monoclinic structures marked in red and black, respectively (for details see Table 2), and $La(OH)_3$ observed in the LaN sample crystallising in hexagonal $P6_3/m$ structure marked in orange. Reflexes arising from Vaseline used to fixate the powders are marked with black stars[75].

behaviour within nitride materials[36]. However, from the analysis of this investigation, this cannot be precisely elucidated.

Figure 3 additionally compares the ΔH_f° for the *Ln*N compounds with that of UN ($\Delta H_f^\circ = -288.8$ kJ mol^{-1}), which was determined by the same methodology on the same experimental instrument[22]. It shows that UN exhibits a less negative enthalpy of formation than all *Ln*N, which aligns well with the observed trend that larger cationic radii[35] of +3 cations in sixfold coordination environment correspond to less negative ΔH_f°.

The Gibbs energy of formation and oxidation stability for LnN and UN compounds in the context of UN based spent nuclear fuel

To summarise thus far, the present investigation has systematically and accurately determined ΔH_f° and high-temperature oxidation chemical reactions of all *Ln*N compounds except for Pm. Considering the relevance of these phases to UN-based SNF, it is salient to discuss their occurrence and associated thermodynamic chemistry with the results of this investigation considered. In UN-based SNF, *Ln*N compounds are expected to form as a major group of fission products that are readily miscible within the UN matrix owing to their shared crystal structure[1,37] and demonstrated solid solution behaviour[9,18,19]. The degree and type of solid solution, for instance, constituents and amounts, significantly impact the properties of UN. For instance, it has been shown for Ce- and Gd-doped UN solid solutions that increasing the amount of Ce-content reduces oxidation resistivity at high temperatures[38]; whereas increasing Gd-content reduces thermal conductivity[39]. At the same time, computational studies of Zr- and Y-doped UN indicate oxidation resistance[40]. In situ steam experiments indicate that Zr-doped UN oxidation resistance also occurs[41]. Although from the literature, a definitive answer as to the stability of UN materials from doping is not present, it is clear that the *Ln* incorporation affects the stability of UN. Such effects are well known for UO_2-based SNF[42] with a strong thermodynamic description behind it[42,43], whereby the incorporation of *Ln* improves

resistance to oxidation. To assess analogous behaviour in UN systems, a thermodynamic framework is required. In this regard, the Gibbs energy of formation as nitrides, ΔG_f°, the Gibbs energy of oxidation to oxide state, ΔG_{ox}°, and the Gibbs energy of hydrolysis to hydroxide/oxide state, ΔG_{hyd}°, are evaluated using the enthalpic data determined from this investigation. Combined with reference entropy values from literature[44–54] ΔG_f°, ΔG_{ox}° and ΔG_{hyd}° can be calculated via the Gibbs equation for all investigated *Ln*N compounds and also in reference to UN when assuming conditions of RT oxidation.

The Gibbs equation, as shown in Eq. (3), uses the reaction enthalpy, ΔH_{rct}° and reaction entropy, ΔS_{rct}°, of a chemical reaction, which are determined via Hess's law shown in Eqs. (4) and (5). This is achieved by subtracting the sum of enthalpies of formation or standard entropies of the reaction products from the sum of the reactants, respectively.

$$\Delta G^\circ = \Delta H_{rct}^\circ - T\Delta S_{rct}^\circ \quad (3)$$

$$\Delta H_{rct}^\circ = \sum \nu\left(\Delta H_f^\circ\right)_{products} - \sum \nu\left(\Delta H_f^\circ\right)_{educts} \quad (4)$$

$$\Delta S_{rct}^\circ = \sum \nu S^\circ{}_{products} - \sum \nu S^\circ{}_{educts} \quad (5)$$

To calculate ΔG_f°, the formation reactions of *Ln*N and UN compounds are required, which are provided in Eqs. (6) and (7). Specifically for the formation of materials as in the present study, $\Delta H_{rct,f}^\circ$ can be replaced by the formation enthalpies determined for *Ln*N and literature data on UN[22]. Reaction formation entropies $\Delta S_{rct,f}^\circ$ are calculated using literature values for all compounds, which are summarised in Supplementary Information Note 4 Table S4. Since the standard entropies S° on pure *Ln*N materials are scarcely known, the available values for LaN and CeN summarised in Supplementary Information Note 4 Table S4 were used as a replacement for all *Ln*N.

$$Ln + \frac{1}{2}N_2 \rightarrow LnN \quad (6)$$

$$U + \frac{1}{2}N_2 \rightarrow UN \quad (7)$$

In order to describe the oxidation stability of *Ln*N and UN compounds via ΔG_{ox}°, a similar thermodynamic methodology is applied. It is assumed that the oxidation occurs in a dry oxygen atmosphere for simplicity, although it was previously shown that *Ln*N compounds react preferably with atmospheric water when contacting with air at room temperature[1]. Given this assumption, the oxidation of *Ln*N is described via the pathways in Eqs. (1) and (2). The oxidation of UN at 298.15 K can be described in a simplified form from literature observations[22,55,56] as shown in Eq. (8).

$$UN + O_2 \rightarrow UO_2 + \frac{1}{2}N_2 \quad (8)$$

ΔH_f° values used to calculate the reaction enthalpy of oxidation $\Delta H_{rct,ox}^\circ$ are summarised in Tables 4 to 6 and Supplementary Information

Table 1 | Lattice parameters determined from Rietveld refinements against PXRD data, associated fitting factors and literature lattice parameters for pristine *Ln*N (*Ln* = La, Ce, Sm, Eu, Er, Yb) phases synthesised

Compound	Structure and space group	Lattice parameter (Å)	Fitting factors (%)	Reference lattice parameter (Å)
LaN	Cubic face centred $Fm\bar{3}m$	a = 5.299240(20)	R = 2.48 R_w = 3.47	a = 5.301(2)[28]
CeN		a = 5.022364(20)	R = 1.10 R_w = 1.60	a = 5.020(2)[28]
SmN		a = 5.047712(26)	R = 2.13 R_w = 2.81	a = 5.046(2)[29]
EuN		a = 5.015175(7)	R = 3.46 R_w = 4.84	a = 5.01779(6)[30]
ErN		a = 4.836127(14)	R = 2.24 R_w = 3.83	a = 4.8481(7)[31]
YbN		a = 4.783650(10)	R = 2.32 R_w = 3.95	a = 4.775(4)[32]

Additional refinement details are provided in Supplementary Information Note 2, Table S2. Note uncertainties are reported directly from the Rietveld analysis with no correction.

Table 2 | Summary of determined crystalline phases arising from the oxidation of LnN (Ln = La, Ce, Sm, Eu, Er and Yb) in air at 900 °C via Rietveld analysis and their respective literature lattice parameters

Compound	Oxidised phase	Structure and space group	Lattice parameters (Å)	Fitting factors (%)	Literature lattice parameter (Å)
LaN	La_2O_3	$P6_3/mmc$ (194)	a = 3.9377(2) c = 6.1388(2)	R = 1.70 R_w = 2.57	a = 3.9381(3) c = 6.1361(6)[66]
CeN	CeO_2	$Fm\bar{3}m$ (225)	a = 5.4142(1)	R = 2.18 R_w = 3.31	a = 5.4178(1)[67]
SmN	Sm_2O_3	$C2/m$ (12)	a = 14.175(2) b = 3.6331(2) c = 8.8574(9) β = 100.189(5)	R = 1.34 R_w = 2.02	a = 14.1975(9) b = 3.6273(3) c = 8.8561(5) β = 99.986(5)[68]
	Sm_2O_3	$Ia\bar{3}$ (206)	a = 10.931(1)		a = 10.9295(5)[69]
EuN	Eu_2O_3	$C2/m$ (12)	a = 14.110(2) b = 3.6061(2) c = 8.8088(9) β = 100.161(5)	R = 1.39 R_w = 2.08	a = 14.1105(2) b = 3.6021(1) c = 8.8080(2) β = 100.037(1)[70]
	Eu_2O_3	$Ia\bar{3}$ (206)	a = 10.869(1)		a = 10.86831(24)[71]
ErN	Er_2O_3	$Ia\bar{3}$ (206)	a = 10.4417(2)	R = 1.89 R_w = 2.62	a = 10.5486(9)[72]
YbN	Yb_2O_3	$Ia\bar{3}$ (206)	a = 10.4378(2)	R = 2.34 R_w = 3.19	a = 10.4281(2)[73]

Additional refinement results provided by the Rietveld software GSAS-II are shown in Supplementary Information Note 2, Table S2. Note that uncertainties are reported directly from the Rietveld analysis with no correction.

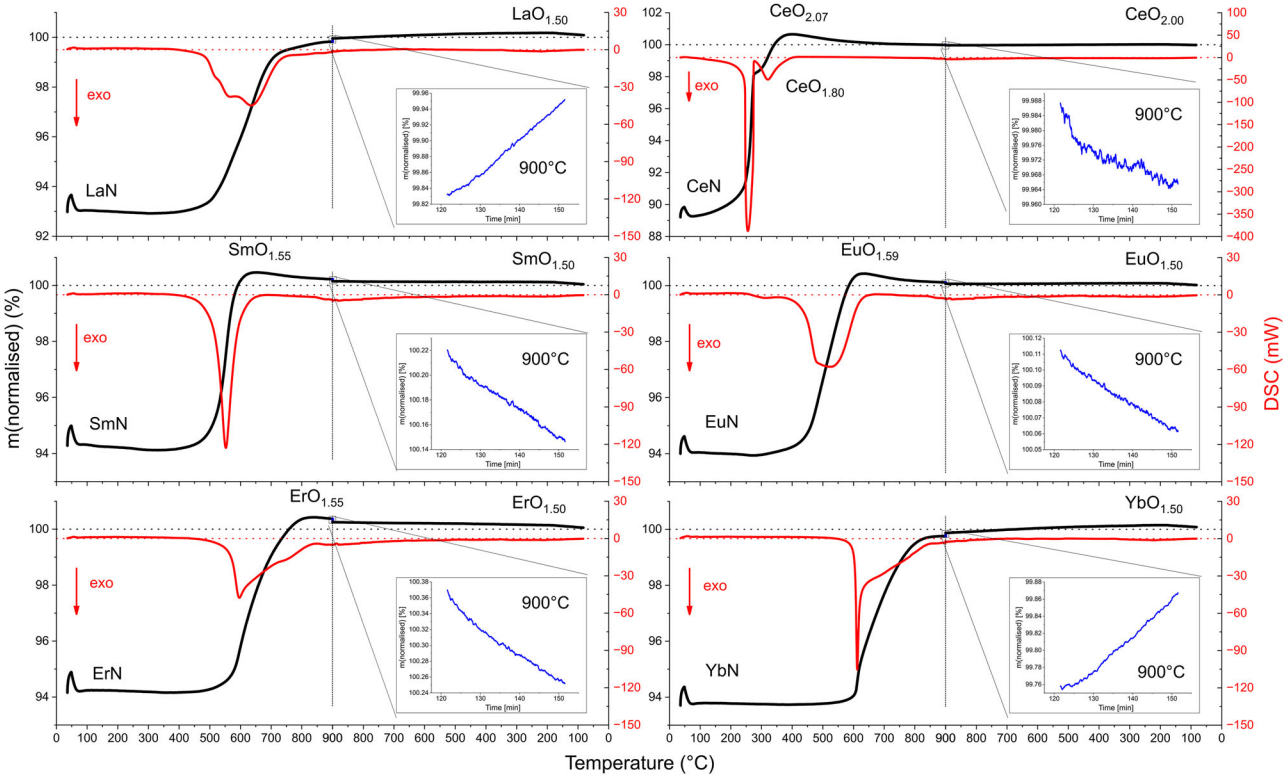


Fig. 2 | TGA profiles for investigated *Ln*N compounds. Combined heating and cooling black TGA- and red DSC curves of LaN, CeN. SmN, EuN, ErN and YbN heated to 900 °C in air with inset blue TGA curve of plateau performed at 900 °C.

Table 3 | Summary of TGA-DSC determined onset temperatures T_{onset} and temperatures of the DSC maxima T_{DSC}, experimental and theoretical mass changes and via PXRD analysis determined oxidation products of *Ln*N (*Ln* = La, Ce, Sm, Eu, Er, Yb) oxidised in air at 900 °C

Compound	T_{onset} (°C) *	T_{DSC} (°C)	Δm_{total} (%)	Δm_{theo} (%) (oxidation product)	Oxidation product
LaN	495.9	566.3 636.41	6.97	6.52 (La_2O_3)	La_2O_3
CeN	175.0	255.7 320.7	11.38	11.66 (CeO_2)	CeO_2
SmN	487.3	552.6	6.14	6.07 (Sm_2O_3)	Sm_2O_3
EuN	420.5	526.3	6.38	6.01 (Eu_2O_3)	Eu_2O_3
ErN	551.7	596.4	6.18	5.50 (Er_2O_3)	Er_2O_3
YbN	603.4	612.1	6.21	5.33 (Yb_2O_3)	Yb_2O_3

All temperature values have an uncertainty of σ = ± 1 °C given by the used thermocouple type S.
*Defined as 5% of total mass change of the nitride to oxide reaction.

Table 4 | Thermochemical cycle used for calculation of ΔH_f° for the *Ln*N compounds where *Ln* = La, Nd, Sm, Eu, Gd, Dy, Ho, Er, Tm, Yb and Lu oxidise to the respective Ln_2O_3, based on drop-solution calorimetric data of the *Ln*N compounds in sodium molybdate at 973 K

Reaction		ΔH (kJ mol^{-1})
(1)	$LnN_{(s,\ 298\ K)} + \frac{3}{2} O_{2(g,\ 973\ K)} \rightarrow \frac{1}{2} Ln_2O_{3(sln,\ 973\ K)} + \frac{1}{2} N_{2(g,\ 973\ K)}$	$\Delta H_1 = \Delta H_{ds}$ *
(2)	$Ln_2O_{3(s,\ 298\ K)} \rightarrow Ln_2O_{3(s,\ 973\ K)}$	ΔH_2 *
(3)	$O_{2(g,\ 298\ K)} \rightarrow O_{2(g,\ 973\ K)}$	$\Delta H_3 = 21.74(2)$[53]
(4)	$N_{2(g,\ 298\ K)} \rightarrow N_{2(g,\ 973\ K)}$	$\Delta H_4 = 20.65$[74]
(5)	$2\ Ln_{(s,\ 298\ K)} + \frac{3}{2} O_{2(g,\ 298\ K)} \rightarrow Ln_2O_{3(s,\ 298\ K)}$	$\Delta H_5 = \Delta H_f^\circ(Ln_2O_3)$ *
Enthalpy of Oxidation *Ln*N → Ln_2O_3		
(6)	$LnN_{(s,\ 298\ K)} + \frac{3}{2} O_{2(g,\ 298\ K)} \rightarrow \frac{1}{2} Ln_2O_{3(s,\ 298\ K)} + \frac{1}{2} N_{2(g,\ 298\ K)}$	
	$\Delta H_{ox} = \Delta H_{ds} + \frac{3}{2}\Delta H_3 - \frac{1}{2}\Delta H_2 - \frac{1}{2}\Delta H_4$	
Enthalpy of Formation *Ln*N		
(7)	$Ln_{(s,\ 298\ K)} + \frac{1}{2} N_{2(g,\ 298\ K)} \rightarrow LnN_{(s,\ 298\ K)}$	
	$\Delta H_f^\circ(LnN) = -\Delta H_{ox} + \frac{1}{2}\Delta H_5$	

The summarised values of dissolution enthalpies ΔH_{ds} and additional enthalpies required are provided in Supplementary Information Note 3, Table S3. Resulting standard enthalpy of formation of *Ln*N are summarised in Table 6.
s = solid, g = gaseous, sln = solution.
*Values summarised in Supplementary Information Note 3, Table S3.

Note 3, Table S3. The standard entropies used to calculate the reaction entropy of oxidation $\Delta S_{rct,ox}^\circ$ for *Ln*N and UN are summarised in Supplementary Information Note 4, Table S4. As described earlier, the standard entropies S° on pure *Ln*N materials are scarcely known; consequently, the available values for LaN and CeN are summarised in Supplementary Information Note 4 Table S4 were used as a replacement for all *Ln*N.

Previously conducted oxidation experiments of *Ln*N in air at RT conditions have revealed that these compounds react via a water-mediated oxidation pathway, resulting in the formation of the complementary $Ln(OH)_3$ as shown in Eq. (9)[1]. Thus, to establish a thermodynamic framework of their oxidation behaviour, the hydrolysis of *Ln*N and UN via ΔG_{hyd}° must also be considered. In this regard, the hydrolysis of UN can be described with respect to the literature as shown Eq. (10)[57–59].

$$LnN + 3\,H_2O \rightarrow Ln(OH)_3 + NH_3 \quad (9)$$

Table 5 | Thermochemical cycle used for calculation of ΔH_f° for the *Ln*N compounds where *Ln* = Ce, Pr, Tb oxidise to the respective $Ln O_2$, based on drop-solution calorimetric data of *Ln*N compounds in sodium molybdate at 973 K

Reaction		ΔH (kJ mol^{-1})
(1)	$LnN_{(s,\ 298\ K)} + O_{2(g,\ 973\ K)} \rightarrow LnO_{2(sln,\ 973\ K)} + \frac{1}{2} N_{2(g,\ 973\ K)}$	$\Delta H_1 = \Delta H_{ds}$ *
(2)	$LnO_{2(s,\ 298\ K)} \rightarrow LnO_{2(s,\ 973\ K)}$	ΔH_2 *
(3)	$O_{2(g,\ 298\ K)} \rightarrow O_{2(g,\ 973\ K)}$	$\Delta H_3 = 21.74(2)$[53]
(4)	$N_{2(g,\ 298\ K)} \rightarrow N_{2(g,\ 973\ K)}$	$\Delta H_4 = 20.65$[74]
(5)	$Ln_{(s,\ 298\ K)} + O_{2(g,\ 298\ K)} \rightarrow LnO_{2(s,\ 298\ K)}$	$\Delta H_5 = \Delta H_f^\circ(LnO_2)$ *
Enthalpy of Oxidation *Ln*N → LnO_2		
(6)	$LnN_{(s,\ 298\ K)} + O_{2(g,\ 298\ K)} \rightarrow LnO_{2(s,\ 298\ K)} + \frac{1}{2} N_{2(g,\ 298\ K)}$	
	$\Delta H_{ox} = \Delta H_{ds} + \Delta H_3 - \Delta H_2 - \frac{1}{2} \Delta H_4$	
Enthalpy of Formation *Ln*N		
(7)	$Ln_{(s,\ 298\ K)} + \frac{1}{2} N_{2(g,\ 298\ K)} \rightarrow LnN_{(s,\ 298\ K)}$	
	$\Delta H_f^\circ(LnN) = - \Delta H_{ox} + \Delta H_5$	

The summarised values of dissolution enthalpies, ΔH_{ds}, and additional enthalpies required are provided in Supplementary Information Note 3, Table S3. Resulting standard enthalpy of formation of *Ln*N are summarised in Table 6.
s = solid, g = gaseous, sln = solution.
*Values summarised in Supplementary Information Note 3, Table S3.

Table 6 | Standard enthalpy of formation ΔH_f° for *Ln*N compounds

Compound	ΔH_f° (kJ mol^{-1})	$\sigma(\Delta H_f^\circ)$ (kJ mol^{-1})
LaN	−316.92	13.1
CeN	−388.35	8.1
PrN	−321.24	15.4
NdN	−375.22	9.0
SmN	−385.98	11.5
EuN	−328.28	7.8
GdN	−368.28	19.4
TbN	−347.28	11.0
DyN	−489.26	12.9
HoN	−517.75	7.3
ErN	−566.98	16.7
TmN	−489.82	11.7
YbN	−529.08	8.1
LuN	−549.71	5.6

Enthalpies are based on performed high-temperature oxide melt calorimetry experiments and their respective two standard errors σ (ΔH_f°).

$$UN + 2H_2O \rightarrow UO_2 + NH_3 + \frac{1}{2} H_2 \quad (10)$$

All hydrolysis calculations were performed assuming that water participating in the hydrolysis was in the gaseous state. The reaction enthalpy of hydrolysis $\Delta H_{rct,hyd}^\circ$ was derived using the formation enthalpies summarised in Tables 4 to 6 and Supplementary Information Note 3, Table S3. The standard entropies used to calculate the reaction entropy of hydrolysis $\Delta S_{rct,hyd}^\circ$ are summarised in Supplementary Information Note 4, Table S4. Once again, given that standard entropies S° on pure *Ln*N materials are scarcely known, entropy values for LaN and CeN were used as a replacement

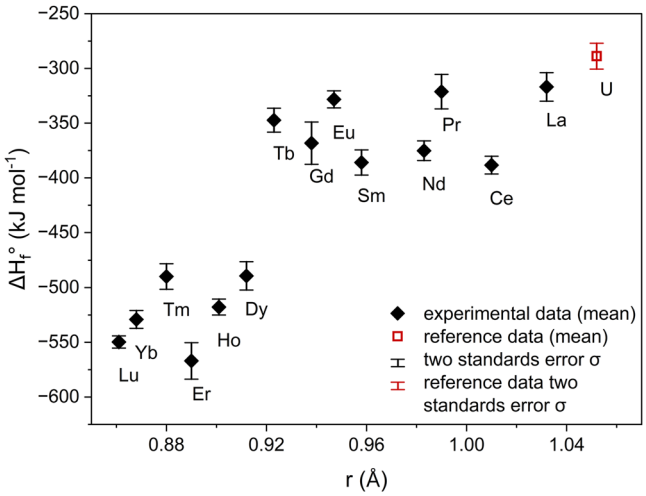


Fig. 3 | Formation Enthalpies of *Ln*N compounds compared against UN. Experimentally determined ΔH_f° of *Ln*N (*Ln* = La, Ce, Pr, Nd, Sm, Eu, Gd, Tb, Dy, Ho, Er, Tm, Yb and Lu) plotted against the ionic radii, r, of the Ln^{3+} cation in 6-fold coordination. The literature ΔH_f° of UN determined by the same methodology is plotted for comparison[22]. Both the experimental and reference data points represent the arithmetic mean with error bars that represent ±2 standard error of the mean.

for all *Ln*N. Additionally, S° for $Lu(OH)_3$ was replaced by the available literature S° of $Tm(OH)_3$[60]. All thermodynamic data that were calculated via the methodology described are summarised in Table 7 and Supplementary Information Note 4, Table S5.

Comparison of the calculated Gibbs energies allows evaluation of the aforementioned stability case scenarios: (a) relative stability of *Ln*N compounds formed within and compared to UN within UN-based SNF, (b) the subsequent stability of UN SNF against oxidation and (c) the stability of UN SNF against hydrolysis, such as what may occur during an unexpected cladding breach. These scenarios are illustrated in Fig. 4a–c, and the calculated ΔG_f°, ΔG_{ox}° and ΔG_{hyd}° values are plotted as a function of ionic radii in Fig. 5a–c, respectively. Note that the schemes assume ideal reaction scenarios, without passivation of phases.

Figure 5a compares calculated ΔG_f° of *Ln*N with UN by plotting them against the ionic radii of the Ln^{3+}/U^{3+} cation in a sixfold coordination environment in the isostructural nitrides crystallising in $Fm\bar{3}m$ structure. At 298.15 K, all *Ln*N exhibit comparable more negative ΔG_f° values than UN, indicating thermodynamically favourable formation of nitrides as described in Eqs. (6) and (7). Consequently, it can be inferred that all *Ln*N compounds examined exhibit a higher stability than UN, implying that a solid solution with UN in UN-based SNF will be stabilised by the presence of secondary fission product *Ln*N phases under the given conditions. It is, however, stressed that this investigation is directed at end member compositions where solid solution measurements are necessary to test the veracity of this postulate. Additionally, *Ln*N compounds with heavier and smaller *Ln* cations exhibit comparable lower ΔG_f° values than *Ln*N compounds with lighter and larger *Ln* cations, which are more closely related to the ΔG_f° calculated for UN. Hence, *Ln*N fission product phases with heavier and smaller *Ln* cations are expected to provide a greater stabilisation effect on the UN matrix. These results also suggest that burnup of UN fuel, through the accumulation of *Ln*-based fission products that are lattice matrix soluble, will affect the thermodynamic stability of UN and suggest an enhancement in the energetic stability of the UN-based SNF matrix.

Scenario b) compares the oxidation of *Ln*N and UN as described in Eqs. (1), (2), and (8) shift the focus to the decomposition of the nitrides in the presence of oxygen. A measure to describe this chemical behaviour is presented by the calculated ΔG_{ox}° plotted in Fig. 5b against the ionic radii of the *Ln*/U cations in the oxide compounds. Unlike Scenario a), the comparison is more complex as the oxides are not isostructural; consequently Table 5 additionally provides the literature ionic radii[35] values of *Ln*/U cations in

their respective oxide structures, considered for plotting ΔG_{ox}° against[35]. From Fig. 5b, it is observed that all *Ln*N compounds have less negative ΔG_{ox}° values than UN, specifically under the given conditions, equivalent to a preferred oxidation of UN over *Ln*N. This result implies that a solid solution of UN with *Ln*N will be stabilised against oxidation, consistent with previous findings[1]. Consistent with Scenario a), heavier *Ln* cations provide an increased stabilising effect, indicating that increasing fission product accumulation from higher burnup enhances the oxidation resistance of UN-based SNF. It should be emphasized that these implications depend on the stated assumptions, particularly variation in temperature and composition of the exposed atmosphere, both of which can have significant effects upon ΔG_{ox}°. Nevertheless, the results of the investigation are consistent with experimental investigations on the stability of doped UN materials[40,41], pointing towards increased thermodynamic and oxidation stability in the occurrence of *Ln*-doped UN.

Recent investigations have shown that in the presence of air containing both atmospheric oxygen and water, *Ln*N compounds oxidise via water to form the respective $Ln(OH)_3$ instead of oxides. Therefore, the hydrolysis reaction must also be considered to establish a thermodynamic perspective on the oxidation behaviour of these compounds. Scenario c) compares the hydrolysis of *Ln*N against UN, as described by Eqs. (9) and (10). As a measure for comparison, the Gibbs energies of hydrolysis ΔG_{hyd}° are presented and plotted in Fig. 5c against the literature ionic radii[35] of *Ln*/U cations in the respective $Ln(OH)_3$ and UO_2. Note that it was shown that $Ln(OH)_3$ resulting from *Ln*N air oxidation forms crystalline structures only for *Ln* = Pr, Nd, while the *Ln* = Gd, Tb, Dy, Ho, Tm, Lu were observed to form amorphous structures[1]. For the present comparison of ΔG_{hyd}° it was assumed that all $Ln(OH)_3$ will be crystallising isostructural in the hexagonal $P6_3/m$ (#176) space group, as observed for $Pr(OH)_3$ and $Nd(OH)_3$[1], in order to choose the ionic radii[35] from literature for the respective *Ln* cation to plot against. From Fig. 5c, it becomes apparent that ΔG_{hyd}° for *Ln*N is comparably higher than for UN, which, given the stated conditions, is equivalent to a preferred hydrolysis of UN over *Ln*N. Similar to the oxidation scenario b), this implies that *Ln*N will have a stabilising effect on the UN matrix. Consistent with scenarios a) and b), the results imply that a higher content of fission products, particularly with heavier *Ln* cations, will increase the hydrolysis stability of UN SNF. This effect correlates with the burnup of the fuel, indicating that a higher burnup increases the hydrolysis resistance. Notably, these implications are strongly based on the stated assumptions and are influenced by the temperature and exact composition of the exposed atmosphere, which can significantly affect ΔG_{hyd}°.

Table 7 | Gibb's energies of formation ΔG_f° for *Ln*N and UN, their oxidation ΔG_{ox}° and their hydrolysis ΔG_{hyd}° at 298.15 K

Compound	ΔG_f° (kJ mol^{-1})	r_{ionic} (*Ln*/U in oxide) (Å)[35]	ΔG_{ox}° (kJ mol^{-1})	r_{ionic} (*Ln*/U in hydroxide) (Å)[35]	ΔG_{hyd}° (kJ mol^{-1})
LaN	−303.90	1.16	−573.31	1.16	−330.12
CeN	−371.59	0.87	−686.21	1.143	−262.14
PrN	−303.15	0.85	−622.64	1.126	−327.63
NdN	−357.97	1.109	−530.44	1.109	−274.91
SmN	−369.21	0.958	−523.42	1.079	−253.94
EuN	−309.03	0.947	−493.76	1.066	−222.37
GdN	−351.97	0.938	−540.43	1.053	−274.18
TbN	−329.37	0.76	−605.45	1.04	−301.60
DyN	−470.88	0.912	−440.22	1.027	−173.80
HoN	−499.33	0.901	−422.66	1.015	−147.93
ErN	−549.11	0.89	−381.35	1.004	−99.67
TmN	−471.71	0.88	−451.10	0.994	−164.80
YbN	−515.19	0.868	−373.46	0.985	−97.59
LuN	−538.47	0.861	−380.63	0.861	−110.81
UN	−283.08	1.00	−779.34	1.00*	−327.17

Calculated using Eqs. (3) to (5), based on the reactions shown in Eqs. (1), (2), and (6) to Eq. (10). Additionally, literature ionic radii[35] of *Ln*/U cations in the oxide/hydroxide materials after oxidation/hydrolysis used to plot the Gibbs energies in Fig. 5 are summarised. Note that the respective ionic radii of the cations were chosen according to their coordination numbers and oxidation states (Ln^{4+} for *Ln* = Ce, Pr, Tb and U^{4+}) in the resulting oxidation product.
* Hydrolysis reaction product = UO_2, see Eq. (10).

Conclusions

High-temperature oxide melt calorimetry experiments were performed to determine ΔH_f° for all *Ln*N compounds (*Ln* = La, Ce, Pr, Nd, Sm, Eu, Gd, Tb, Dy, Ho, Er, Tm, Yb, Lu; excluding Pm) which are isostructural. A clear trend is observed whereby the ΔH_f° of *Ln*N compounds with larger and lighter *Ln* exhibits more negative values than those of *Ln*N with smaller and heavier *Ln*. A distinct discontinuity observed in ΔH_f° further highlights the role of 4*f* electrons in governing thermodynamic stability. Comparison with isostructural UN, for which ΔH_f° was determined using the same methodology previously[22], further supports these trends. Due to the relevance of UN and *Ln*N compounds to UN-based SNF, ΔG_f°, ΔG_{ox}° and ΔG_{hyd}° were derived based on the results of this work and literature data. These analyses suggest that *Ln*N compounds exhibit generally higher chemical stability compared to UN, and the presence of potential UN-*Ln*N solid-solution phases within SNF will enhance structural stability and oxidation resistance during irradiated and air-cladding breach scenarios.

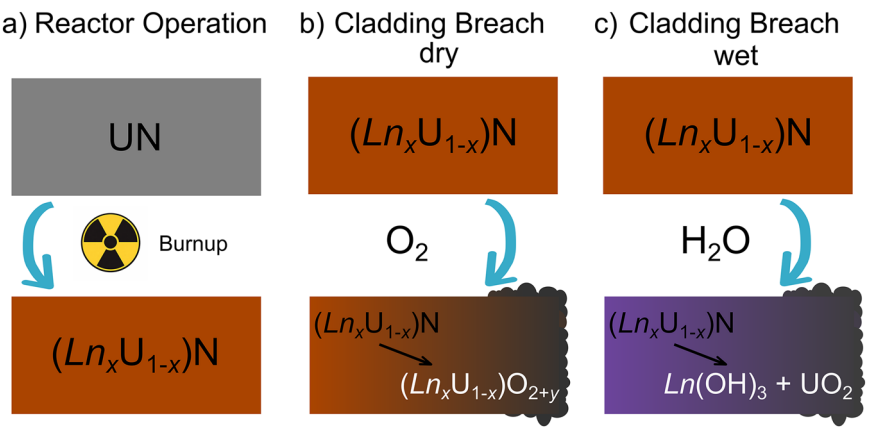


Fig. 4 | Stability scenarios for UN based SNF. Schematic illustration of ideal stability case scenarios comparing (**a**) formation of *Ln*N against UN in UN based SNF during irradiation, (**b**) oxidation of *Ln*N against UN in a cladding breach scenario involving oxygen-fuel contact and (**c**) hydrolysis of *Ln*N against UN in a cladding breach scenario involving water-fuel contact under RT conditions.

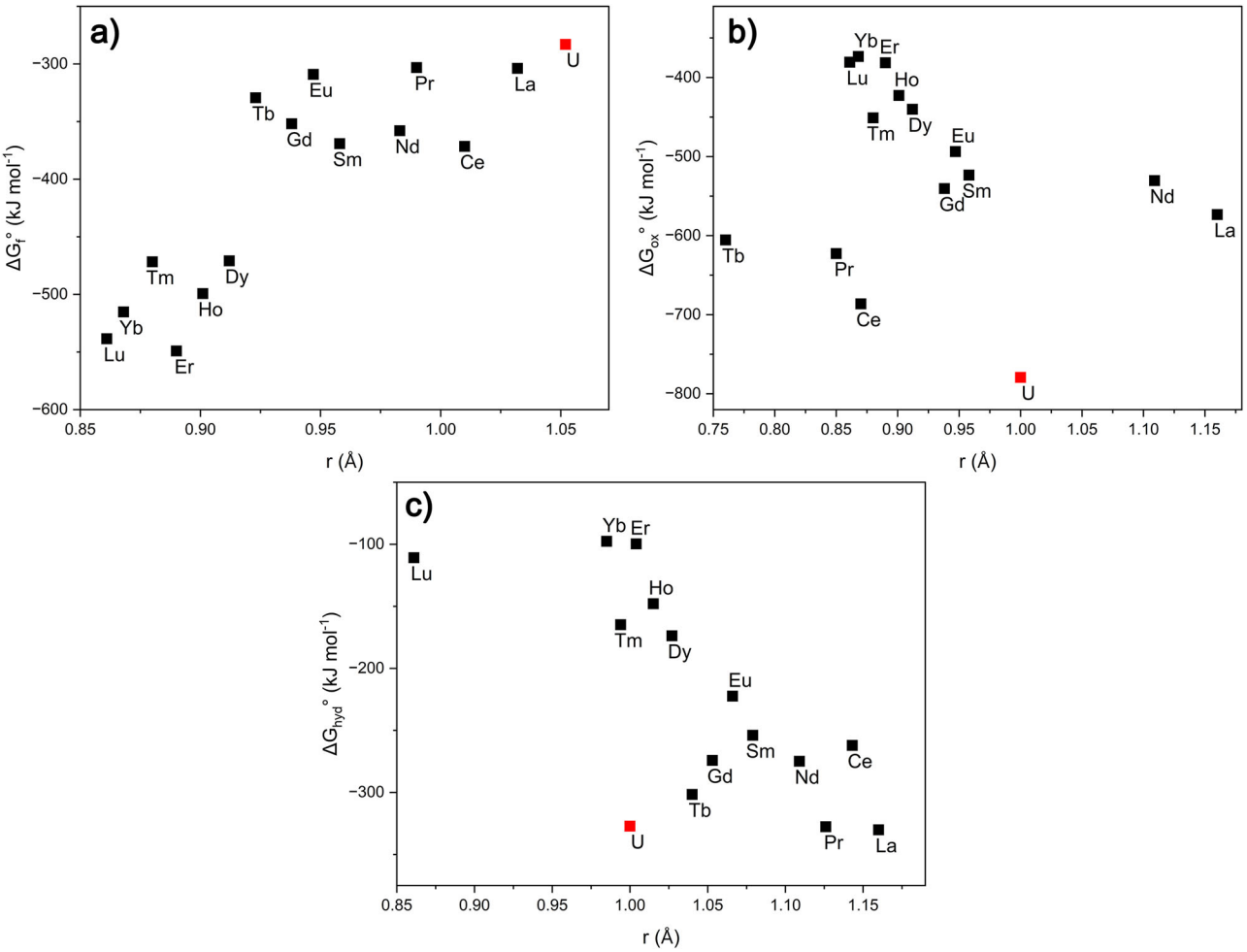


Fig. 5 | Comparison of Gibbs energies for formation ΔG_f°, oxidation ΔG_{ox}° and hydrolysis ΔG_{hyd}° of investigated *Ln*N compounds against UN. Gibbs energies of (**a**) formation ΔG_f° for *Ln*N and UN, (**b**) oxidation ΔG_{ox}° for *Ln*/U oxides (Ln_2O_3 for *Ln* = La, Nd, Sm, Eu, Gd, Dy, Ho, Er, Tm, Lu; LnO_2 for *Ln* = Ce, Pr, Tb) and (**c**) hydrolysis ΔG_{hyd}° for $Ln(OH)_3/UO_2$ plotted against the ionic radii[35] of the *Ln*/U cation in the respective compound. All Gibbs energies are calculated for 298.15 K as shown in Eqs. (3) to (5), based on the chemical reactions described for the formation of *Ln*N and UN see Eqs. (6) and (7), as well as their oxidation in Eqs. (1), (2), (8) and Eqs. (9) to (10). The Gibbs energies and literature ionic radii of varying oxide/hydroxide structures used for plotting are summarised in Table 7. Note that the respective ionic radii of the cations were chosen according to their coordination numbers and oxidation states (Ln^{4+} for *Ln* = Ce, Pr, Tb and U^{4+}) in the resulting oxidation product.

Moreover, the work provides critical thermodynamic data for *Ln*N systems, advancing the understanding of UN-based SNF, and offering broader insights into general nitride materials that can be found in advanced technology applications like fusion energy and thermoelectric in which *Ln*N compounds play a fundamental role.

Methods

Synthesis

The synthesis and utilisation of the *Ln*N powders used in the investigation are derived from a previous study[1]. A direct nitridation approach was used, in which fine pieces of lanthanide metals (Hunan Rare Earth Metals Materials Co, 99.9%) were heated in a flowing nitrogen atmosphere (Nippon Gases, 99.999%, purified with an oxysorb cartridge) utilising a custom water-cooled radio frequency furnace[61]. After the complete reaction of the samples, they were crushed and sieved through a 100 mesh. The preparation of samples was carried out in a protective argon atmosphere.

Powder X-ray diffraction

PXRD data of finely ground *Ln*N powders was collected on a Huber G670 imaging plate Guinier camera ($2\Theta_{max} = 100°$) using a curved germanium (111) monochromator and Cu-$K_{\alpha1}$ (*Ln* = La, Ce, Sm, Er, Yb) or Co-$K_{\alpha1}$ radiation (*Ln* = Eu) at 293(1) K. Co-$K_{\alpha1}$ radiation was used for EuN to avoid fluorescence effects that are caused by the Cu-$K_{\alpha1}$ energy alike L_1-edge of Eu, hence improving the signal to noise ratio of the diffraction data[62,63]. The powder samples were placed between Kapton foils to avoid oxidation in air. PXRD data of the high-temperature oxidised *Ln*N (*Ln* = La, Ce, Sm, Eu, Er, Yb) compounds in this investigation were collected on a Bruker D8 diffractometer equipped with a Lynxeye XE-T detector in Bragg–Brentano configuration using Cu-$K_{\alpha1,2}$ radiation (λ = 1.54184 Å) at room temperature. The powder samples were placed on a thin Vaseline layer on Si-zero background holders closed by an airtight Kapton dome. Measurements were performed in the range of $20° \le 2\theta \le 85°$ with a step size of $(2\theta) = 0.02°$ and a counting time of 2 s per step. Data analysis was performed via the Rietveld method as implemented in the program GSAS-II[64]. The PXRD characterisation of pristine and high-temperature oxidised *Ln*N powders (*Ln* = Pr, Nd, Gd, Tb, Dy, Ho, Tm, Lu) was reported previously[1].

Thermogravimetric analysis

The thermogravimetric characterisation of the high-temperature oxidation behaviour of *Ln*N (*Ln* = La, Ce, Sm, Eu, Er, Yb) powders with a NETZSCH

STA 449C in thermogravimetric and differential scanning calorimetry setup (TGA-DSC) equipped with a thermocouple type S ($\sigma_T = \pm 1$ °C) has been adapted from previous works[1]. Powder samples of 20 mg were heated in Pt/Rh crucibles (NETZSCH) to 900 °C under flowing synthetic air at 10 °C/min rate. The oxidation residues were analysed by PXRD.

High temperature oxide melt drop solution calorimetry

High temperature calorimetry experiments were performed using a Calvet Calorimeter (Setaram AlexSys 1000)[34,65], where each of the two calorimeter chambers was maintained at 973 K and contained a quartz crucible with 30 g of molten sodium molybdate solvent ($3\ NaO \cdot 4\ MO_3$). The sample chambers were kept under flowing oxygen gas (A-L Compressed Gases, 99.5%) with ~60 mL/min, which was also bubbled through molten salt solvents at 4 mL/min to maintain oxidising conditions. Prior to sample measurements, the calorimeter was calibrated using Al_2O_3 calibrants, which were dropped into empty quartz crucibles in separate experimental runs. Pellets of around 5 mg *Ln*N (*Ln* = La, Ce, Pr, Nd, Sm, Eu, Gd, Tb, Dy, Ho, Er, Tm, Yb, Lu) with a diameter of 1 mm were prepared before each respective experiment and sealed in plastic bags under a protective nitrogen atmosphere. In order to minimise air contact of the sample pellets, the bags were cut open right before the drop into the calorimeter, where they dissolved in the molten salt solvent. During the initial drop experiments of CeN, visible light flashes were observed, indicating ignition before dissolution. To prevent unintended oxidation, CeN samples were encapsulated in Rutile-structured TiO_2 pellets (1.5 mm diameter), isolating them from air contact until dissolution. PXRD structure analysis of TiO_2 is provided in Supplementary Information Note 1, Fig. S1 with Rietveld analysis results summarised in Table S1. The standard enthalpy of formation was calculated by two constructed thermocycles which were based on the observed high-temperature oxidation behaviour for the respective *Ln*N compounds described in this investigation and elsewhere[1].

Data availability

The data that support the findings of this study is available in an open access Zenodo repository, https://doi.org/10.5281/zenodo.22296171.

Received: 19 May 2026; Accepted: 18 September 2026;
Published online: 07 October 2026

References

1. Uhlemann, P. et al. The ambient- and high-temperature oxidation behaviour of $U^{3+}N$ and $Ln^{3+}N$ compounds relevant to spent nuclear fuel. https://doi.org/10.1038/s41529-026-00827-3 (2026).
2. Holmes-Hewett, W. F., Miller, J. D., Ahmad, H. G., Granville, S. & Ruck, B. J. Rare-earth nitrides: fundamental advances and applications in cryogenic electronics. *J. Phys. D Appl. Phys.* **58**, 343001 https://doi.org/10.1088/1361-6463/adf1b2 (2025).
3. Xiao, K., Shi, X., Zhang, X., Ping, Q. & Du, L. The emergence of novel magnetic properties in ternary iron nitrides toward spintronics: first-principles calculations. *Phys. Chem. Chem. Phys.* **27**, 6677–6686 https://doi.org/10.1039/d5cp00405e (2025).
4. Kwon, H. R., Yang, J. W. & Jang, H. W. Metal nitride catalysts for photoelectrochemical and electrochemical catalysis. *Exploration* **5**, 20240013 https://doi.org/10.1002/exp.20240013 (2025).
5. Porter, W. N., Turaczy, K. K., Yu, M., Mou, H. & Chen, J. G. Transition metal nitride catalysts for selective conversion of oxygen-containing molecules. *Chem. Sci.* **15**, 6622–6642 https://doi.org/10.1039/d4sc01314j (2024).
6. Fahrenholtz, W. G. & Hilmas, G. E. Ultra-high temperature ceramics: Materials for extreme environments. *Scr. Mater.* **129**, 94–99 https://doi.org/10.1016/j.scriptamat.2016.10.018 (2017).
7. Wan, Y. et al. A nitride-reinforced NbMoTaWHfN refractory high-entropy alloy with potential ultra-high-temperature engineering applications. *Engineering* **30**, 110–120 https://doi.org/10.1016/j.eng.2023.06.008 (2023).
8. Degueldre, C., Goddard, D., Berhane, G., Simpson, A. & Boxall, C. Simulation of uranium mononitride spent fuel: A thermodynamic approach. *J. Nuclear Mater.* 154900 https://doi.org/10.1016/j.jnucmat.2024.154900 (224).
9. Smailos, E. *Reactions of Fission Products in Carbide and Nitride Fuel Based on Simulated Experiments*. Report No. KFK 1953, (Kernforschungszentrum Karlsruhe, 1974).
10. Giacchetti, G., Sari, C. & Walker, C. T. Actinides and fission products distribution in fast breeder nitride fuel. *Nucl. Technol.* **28**, 216–225 https://doi.org/10.13182/nt76-a31562 (1976).
11. Dehlin, F., Wallenius, J. & Bortot, S. An analytic approach to the design of passively safe lead-cooled reactors. *Ann. Nucl. Energy* **169**, 108971. https://doi.org/10.1016/j.anucene.2022.108971 (2022).
12. Dehlin, F., Pallarès Abril, E. & Wallenius, J. Performance and safety evaluation of a < 10 wt% 235U enriched small lead-cooled fast reactor. *Ann. Nucl. Energy* **212**, 110861 (2025).
13. Elkhawas, N. A., Reda, S. M., Amin, E. A. & Anwar, D. Deployment study of accident tolerant fuels in small modular advanced high temperature reactor. *Phys. Scr.* **100**, 095307 https://doi.org/10.1088/1402-4896/ae05d3 (2025).
14. Murphy, G. L. et al. Deconvoluting Cr states in Cr-doped UO_2 nuclear fuels via bulk and single crystal spectroscopic studies. *Nat. Commun.* **14**, 2455 https://doi.org/10.1038/s41467-023-38109-0 (2023).
15. Murphy, G. L. et al. The lattice contraction of UO_2 from Cr doping as determined via high resolution synchrotron X-ray powder diffraction. *J. Nucl. Mater.* **595**, 155046 https://doi.org/10.1016/j.jnucmat.2024.155046 (2024).
16. Murphy, G. L. et al. The role of redox and structure on grain growth in Mn-doped UO_2. *Commun. Mater.* **5**, 274 https://doi.org/10.1038/s43246-024-00714-x (2024).
17. Mishchenko, Y., Johnson, K. D., Jädernäs, D., Wallenius, J. & Lopes, D. A. Uranium nitride advanced fuel: an evaluation of the oxidation resistance of coated and doped grains. *J. Nucl. Mater.* **556**, 153249 (2021).
18. Holleck, H., Smailos, E. & Thümmler, F. Zur Mischkristallbildung von UN mit den Nitriden der Seltenen Erden CeN und NdN. *J. Nucl. Mater.* **28**, 105–109 https://doi.org/10.1016/0022-3115(68)90061-5 (1968).
19. Holleck, H., Smailos, E. & Thümmler, F. Zur Mischphasenbildung der Mononitride in den Systemen U- (Y, La, Pr)-N. *J. Nucl. Mater.* **32**, 281–289 https://doi.org/10.1016/0022-3115(69)90077-4 (1969).
20. Klipfel, M., Di Marcello, V., Schubert, A., van de Laar, J. & van Uffelen, P. Towards a multiscale approach for assessing fission product behaviour in UN. *J. Nucl. Mater.* **442**, 253–261 https://doi.org/10.1016/j.jnucmat.2013.08.056 (2013).
21. Uno, M., Kurosaki, K., Yamanaka, S. & Minato, K. Thermal properties of simulated high burn up nitride fuels and nitride ADS targets. *MRS Proc.* 1043. https://doi.org/10.1557/proc-1043-t13-03 (2008).
22. Goncharov, V. G. et al. Energetics of oxidation and formation of uranium mononitride. *J. Nucl. Mater.* **569**, 153904. https://doi.org/10.1016/j.jnucmat.2022.153904 (2022).
23. Brown, R. C. & Clark, N. J. Knudsen cell vaporization of rare earth nitrides. Enthalpy of vaporization of holmium nitride ($HoN_{0.98}$). *High. Temp. Sci.* **7**, 131–141 (1975).
24. Brown, R. C. & Clark, N. J. Knudsen cell vaporization of rare earth nitrides: enthalpy of vaporization of samarium(iii) nitride and yttrium nitride. *High. Temp. Sci.* **10**, 17–84 (1978).
25. Kordis, J. & Gingerich, K. A. Heats of vaporization and standard heats of formation of rare earth mononitrides. *J. Nucl. Mater.* **66**, 197–199 https://doi.org/10.1016/0022-3115(77)90147-7 (1977).
26. Dell, R. M. & Wheeler, V. J. The ignition of uranium mononitride and uranium monocarbide in oxygen. *J. Nucl. Mater.* **21**, 328–336 https://doi.org/10.1016/0022-3115(67)90185-7 (1967).

27. Ikawa, K. & Taketani, K. Room temperature oxidation of UN powder. *J. Nucl. Sci. Technol.* **7**, 433–438 https://doi.org/10.1080/18811248.1970.9734717 (1970).
28. Olcese, G. L. Interconfiguration fluctuation of cerium in CeN as a function of temperature and pressure. *J. Phys. F Met. Phys.* **9**, 569–578 https://doi.org/10.1088/0305-4608/9/3/018 (1979).
29. Klemm, W. & Winkelmann, G. Zur Kenntnis der Nitride der Seltenen Erdmetalle. *Z. für. Anorganische und Allg. Chem.* **288**, 87–90 https://doi.org/10.1002/zaac.19562880112 (1956).
30. Suehiro, T., Hirosaki, N., Wada, T., Yajima, Y. & Mitomo, M. Europium nitride synthesized by direct nitridation with ammonia. *Powder Diffr.* **20**, 40–42 https://doi.org/10.1154/1.1835963 (2005).
31. Klesnar, H. & Rogl, P. F. Phase relations in the ternary systems rare-earth metal (*RE*)-boron-nitrogen, where *RE*=Tb, Dy, Ho, Er, Tm., Lu, Sc., Y. *High. Temp. High. Press.* **22**, 453–457 (1990).
32. Doenni, A., Fischer, P., Furrer, A., Bacsa, W. & Wachter, P. F.c.c. type-III antiferromagnetism in YbN. *Z. Fuer Phys. B Condens. Matter* **80**, 269–274 https://doi.org/10.1007/bf01357513 (1990).
33. Kneisel, K. et al. Synthesis, structural, and raman investigation of lanthanide nitride powders (*Ln* = La, Ce, Nd, Sm, Gd, Tb, Dy, Er, Lu). *ACS Omega* **9**, 47842–47847 https://doi.org/10.1021/acsomega.4c08638 (2024).
34. Navrotsky, A. Progress and new directions in calorimetry: a 2014 perspective. *J. Am. Ceram. Soc.* **97**, 3349–3359 https://doi.org/10.1111/jace.13278 (2014).
35. Shannon, R. D. Revised effective ionic radii and systematic studies of interatomic distances in halides and chalcogenides. *Acta Crystallogr. Sect. A* **32**, 751–767 https://doi.org/10.1107/s0567739476001551 (1976).
36. Greenaway, A. L. et al. Ternary nitride materials: fundamentals and emerging device applications. *Annu. Rev. Mater. Res.* **51**, 591–618 https://doi.org/10.1146/annurev-matsci-080819-012444 (2021).
37. Degueldre, C., Goddard, D. T., Berhane, G., Simpson, A. & Boxall, C. Simulation of uranium mononitride spent fuel: a crystallographic approach. *J. Nucl. Mater.* **562**, 153612. https://doi.org/10.1016/j.jnucmat.2022.153612 (2022).
38. Dehadraya, J. V. et al. The oxidation of uranium-cerium mononitride microspheres. *J. Alloy. Compd.* **257**, 313–321 https://doi.org/10.1016/s0925-8388(97)00010-8 (1997).
39. Kim, G. & Ahn, S. Thermal conductivity of gadolinium added uranium mononitride fuel pellets sintered by spark plasma sintering. *J. Nucl. Mater.* **546**, 152785. https://doi.org/10.1016/j.jnucmat.2021.152785 (2021).
40. Yang, S. et al. Atomic-scale insights into oxidation of Zr- and Y-doped UN surfaces and grain boundaries in steam: a first-principles study. *Surf. Interfaces* **65**, 106490. https://doi.org/10.1016/j.surfin.2025.106490 (2025).
41. Stansby, J. H. et al. Enhanced steam oxidation resistance of uranium nitride nuclear fuel pellets. *Corros. Sci.* **230**, 111877. https://doi.org/10.1016/j.corsci.2024.111877 (2024).
42. Liu, J. et al. Non-stoichiometric and Subnano-heterogeneous Ln-incorporated UO_2: its defect chemistry and thermal oxidation. Preprint at https://arxiv.org/abs/2412.03501 (2024).
43. Vinograd, V. L., Bukaemskiy, A. A., Deissmann, G. & Modolo, G. Thermodynamic model of the oxidation of *Ln*-doped UO_2. *Sci. Rep.* **13**, 17944. https://doi.org/10.1038/s41598-023-42616-x (2023).
44. Barin, I. *Thermochemical Data of Pure Substances* (Wiley, 1995).
45. Justice, B. H. & Westrum, E. F. Thermophysical properties of the lanthanide oxides. I. Heat capacities, thermodynamic properties, and some energy levels of Lanthanum(III) and Neodymium(III) oxides from 5 to 350K. *J. Phys. Chem.* **67**, 339–345 https://doi.org/10.1021/j100796a031 (1963).
46. Konings, R. J. M. et al. The thermodynamic properties of the f -elements and their compounds. Part 2. The lanthanide and actinide oxides. *J. Phys. Chem. Ref. Data* **43** https://doi.org/10.1063/1.4825256 (2014).
47. Justice, B. H. & Westrum, E. F. Thermophysical properties of the lanthanide oxides. II. Heat capacities, thermodynamic properties, and some energy levels of Samarium(III), Gadolinium(III), and Ytterbium(III) oxides from 10 to 350°K. *J. Phys. Chem.* **67**, 345–351 https://doi.org/10.1021/j100796a032 (1963).
48. Lyutsareva, N. S., Berezovskii, G. A. & Paukov, I. E. Heat capacity of two modifications of Eu_2O_3 with a range of 8–300 K. *Zh. Fiz. Khim* **68**, 1179–1182 (1994).
49. Konings, R. J. M., van Miltenburg, J. C. & van Genderen, A. C. G. Heat capacity and entropy of monoclinic Gd_2O_3. *J. Chem. Thermodyn.* **37**, 1219–1225 https://doi.org/10.1016/j.jct.2005.02.014 (2005).
50. Westrum, E. F. & Justice, B. H. Thermophysical properties of the lanthanide oxides. III. Heat capacities, thermodynamic properties, and some energy levels of Dysprosium(III), Holmium(III) and Erbium(III) oxides. *J. Phys. Chem.* **67**, 659–665 https://doi.org/10.1021/j100797a029 (1963).
51. Justice, B. H., Westrum, E. F., Chang, E. & Radebaugh, R. Thermophysical properties of the lanthanide oxides. IV. Heat capacities and thermodynamic properties of thulium(III) and lutetium(III) oxides. Electronic energy levels of several lanthanide(III) ions. *J. Phys. Chem.* **73**, 333–340 https://doi.org/10.1021/j100722a010 (1969).
52. Counsell, J. F., Dell, R. M. & Martin, J. F. Thermodynamic properties of uranium compounds. Part 2.—Low-temperature heat capacity and entropy of three uranium nitrides. *Trans. Faraday Soc.* **62**, 1736–1747 https://doi.org/10.1039/tf9666201736 (1966).
53. Robie, R. A. & Hemingway, B. S. *Thermodynamic Properties of Minerals and Related Substances at 298.15 K and 1 bar (10^5 pascals) Pressure and at Higher Temperatures* (United States Government Publishing Office, 1995).
54. Cox, J. D., Wagman, D. D., & Medvedev, V. A. *CODATA Key Values for Thermodynamics* (Hemisphere Publishing Cooperation, 1989).
55. Dell, R. M., Wheeler, V. J. & McIver, E. J. Oxidation of uranium mononitride and uranium monocarbide. *Trans. Faraday Soc.* **62**, 3591 https://doi.org/10.1039/tf9666203591 (1966).
56. Paljević, M. & Despotović, Z. Oxidation of uranium mononitride. *J. Nucl. Mater.* **57**, 253–257 https://doi.org/10.1016/0022-3115(75)90208-1 (1975).
57. Dell, R. M., Wheeler, V. J. & Bridger, N. J. Hydrolysis of uranium mononitride. *Trans. Faraday Soc.* **63**, 1286 https://doi.org/10.1039/tf9676301286 (1967).
58. Watkins, J. K., Butt, D. P. & Jaques, B. J. Microstructural degradation of UN and UN-UO_2 composites in hydrothermal oxidation conditions. *J. Nucl. Mater.* **518**, 30–40 https://doi.org/10.1016/j.jnucmat.2019.02.027 (2019).
59. Sugihara, S. & Imoto, S. Hydrolysis of uranium nitrides. *J. Nucl. Sci. Technol.* **6**, 237–242 https://doi.org/10.1080/18811248.1969.9732878 (1969).
60. Diakonov, I. I., Ragnarsdottir, K. V. & Tagirov, B. R. Standard thermodynamic properties and heat capacity equations of rare earth hydroxides. *Chem. Geol.* **151**, 327–347 https://doi.org/10.1016/s0009-2541(98)00088-6 (1998).
61. Schnick, W., Huppertz, H. & Lauterbach, R. High temperature syntheses of novel nitrido- and oxonitrido-silicates and sialons using rf furnaces. *J. Mater. Chem.* **9**, 289–296 https://doi.org/10.1039/a803900c (1999).
62. Elam, W. T., Ravel, B. D. & Sieber, J. R. A new atomic database for X-ray spectroscopic calculations. *Radiat. Phys. Chem.* **63**, 121–128 https://doi.org/10.1016/S0969-806X(01)00227-4 (2002).
63. Deslattes, R. D. et al. X-ray transition energies: new approach to a comprehensive evaluation. *Rev. Mod. Phys.* **75**, 35–99 https://doi.org/10.1103/RevModPhys.75.35 (2003).

64. Toby, B. H. & Dreele, R. B. v. GSAS-II: the genesis of a modern open-source all purpose crystallography software package. *J. Appl. Crystallogr.* **46**, 544–549 https://doi.org/10.1107/s0021889813003531 (2013).
65. Levchenko, A., Marchin, L., Parlouer, P. L. & Navrotsky, A. The new high-temperature Setaram AlexSYS calorimeter and thermochemistry of alpha-$CuMnO_4$. *ITAS Bull.* **2**, 91–97 (2009).
66. Aldebert, P. & Traverse, J. P. Etude par diffraction neutronique des structures de haute temperature de La_2O_3 et Nd_2O_3. *Mater. Res. Bull.* **14**, 303–323 https://doi.org/10.1016/0025-5408(79)90095-3 (1979).
67. Ma, Y. et al. Introducing highly redox-active atomic centers into insertion-type electrodes for lithium-ion batteries. *Adv. Energy Mater.* **10**. https://doi.org/10.1002/aenm.202000783 (2020).
68. Schleid, T. & Meyer, G. Single crystals of rare earth oxides from reducing halide melts. *J. Less Common Met.* **149**, 73–80 https://doi.org/10.1016/0022-5088(89)90472-4 (1989).
69. Mitric, M. et al. Magnetic properties of trivalent Sm ions in $Sm_xY_{2-x}O_3$. *J. Alloy. Compd.* **485**, 473–477 https://doi.org/10.1016/j.jallcom.2009.05.142 (2009).
70. Yakel, H. L. A refinement of the crystal structure of monoclinic europium sesquioxide. *Acta Crystallogr. Sect. B Struct. Crystallogr. Cryst. Chem.* **35**, 564–569 https://doi.org/10.1107/s0567740879004167 (1979).
71. Heiba, Z. K., Akin, Y., Sigmund, W. & Hascicek, Y. S. X-ray structure and microstructure determination of the mixed sesquioxides $(Eu_{1-x}Yb_x)_2O_3$ prepared by a sol–gel process. *J. Appl. Crystallogr.* **36**, 1411–1416 https://doi.org/10.1107/s0021889803019319 (2003).
72. Heiba, Z. K., Mohamed, M. B. & Fuess, H. Effect of Mn doping on structural and magnetic susceptibility of C-type rare earth nano oxides $Er_{2-x}Mn_xO_3$. *Mater. Res. Bull.* **47**, 4278–4282 https://doi.org/10.1016/j.materresbull.2012.09.018 (2012).
73. Vasundhara, K. et al. Structural and oxide ion conductivity studies on $Yb_{1-x}Bi_xO_{1.5}$ ($0.00 \leqslant x \leqslant 0.50$) composites. *J. Alloy. Compd.* **596**, 151–157 https://doi.org/10.1016/j.jallcom.2014.01.201 (2014).
74. Chase, M. W. Jr, Davies, C. A., Downey, J. R. Jr, Frurip, D. J., McDonald, R. A. & Syverud, A. N. JANAF thermochemical tables: third edition. *J. Phys. Chem. Ref. Data* **14**, 1–1856 (1985).
75. Mârza, S. M. et al. The impact of composites with silicate-based glasses and gold nanoparticles on skin wound regeneration. *Molecules* **26**. https://doi.org/10.3390/molecules26030620 (2021).

Acknowledgements

The authors thank Marianne Feldmann for her support in organising the funding of the HITEC Graduate School. The authors thank Dr. Andreas Wilden for his continuous support by providing and maintaining the function of a glovebox workspace necessary to perform the sample preparations of parts of this work.

Author contributions

The research methodology, experimental planning and formal analysis was developed and conducted by Pascal Uhlemann, Xiaofeng Guo and Gabriel L. Murphy. Funding acquisition and project management was performed by Pascal Uhlemann, C. Schreinemachers, Giuseppe Modolo and Gabriel L. Murphy. The materials were synthesised by Pascal Uhlemann and Peter Höhn. PXRD measurements and analysis were performed by Pascal Uhlemann, Philip Kegler and Peter Höhn. Thermogravimetric measurements were performed by Pascal Uhlemann and Christian Schreinemachers. High temperature calorimetry experiments were conducted by Pascal Uhlemann, Will Vance with support and guidance provided by Matthew P. Heaney and Natalie Yaw. Data analysis and visualisation of the calorimetry experiments, as well as calculations were performed by Pascal Uhlemann, Will Vance and Xiaofeng Guo. Manuscript writing, review and editing was performed by Pascal Uhlemann and Gabriel L. Murphy with input from all authors.

Funding

Financial support for this research was provided by European Commission through the "Fuel Recycle and Experimentally Demonstrated Manufacturing of Advanced Nuclear Solutions for Safety" (FREDMANS) project, grant agreement number 101060800. Views and opinions expressed are those of the authors only and do not necessarily reflect those of the European Union, European Commission or European Atomic Energy Community (granting authority). Neither the European Union nor the granting authority can be held responsible for them. Funding for P. Uhlemann to perform the experimental work in the facilities of Washington State University (WSU) was provided by the HITEC Graduate School of Forschungszentrum Jülich GmbH. Calorimetric work performed at WSU were supported by the United States Nuclear Regulatory Commission, Office of Nuclear Regulatory Research (RES) under award No. 31310023M0011. Open Access funding enabled and organized by Projekt DEAL.

Competing interests

The authors declare no competing interests.

Additional information

Supplementary information The online version contains supplementary material available at https://doi.org/10.1038/s42004-026-02236-8.

Correspondence and requests for materials should be addressed to P. Uhlemann, X. Guo or G. L. Murphy.

Peer review information *Communications Chemistry* thanks all reviewer(s) for their contribution to the peer review of this work. A peer review file is available.

Reprints and permissions information is available at http://www.nature.com/reprints

Publisher's note Springer Nature remains neutral with regard to jurisdictional claims in published maps and institutional affiliations.

Open Access This article is licensed under a Creative Commons Attribution 4.0 International License, which permits use, sharing, adaptation, distribution and reproduction in any medium or format, as long as you give appropriate credit to the original author(s) and the source, provide a link to the Creative Commons licence, and indicate if changes were made. The images or other third party material in this article are included in the article's Creative Commons licence, unless indicated otherwise in a credit line to the material. If material is not included in the article's Creative Commons licence and your intended use is not permitted by statutory regulation or exceeds the permitted use, you will need to obtain permission directly from the copyright holder. To view a copy of this licence, visit http://creativecommons.org/licenses/by/4.0/.

© The Author(s) 2026